Chemical Science

ROYAL SOCIETY OF CHEMISTRY

EDGE ARTICLE

View Article Online
View Journal | View Issue

Check for updates

Cite this: *Chem. Sci.*, 2024, **15**, 14415

All publication charges for this article have been paid for by the Royal Society of Chemistry

Received 10th June 2024
Accepted 8th August 2024

DOI: 10.1039/d4sc03805c

rsc.li/chemical-science

# Slightly Li-enriched chemistry enabling super stable $LiNi_{0.5}Mn_{0.5}O_2$ cathodes under extreme conditions†

Siqi Chen,[a] Ping Zhang,[a] Xin Zhou,[a] Wenbin Wu,[a] Xiaohong Liu,*[a] Yifeng Liu,[b] Guilin Feng,[c] Bin Zhang,[d] Wangyan Xing,[d] Meihua Zuo,[d] Ping Zhang,[d] Genpin Lv,[e] Yao Xiao,*[b] Shixue Dou[f] and Wei Xiang*[ag]

High voltage/high temperature operation aggravates the risk of capacity attenuation and thermal runaway of layered oxide cathodes due to crystal degradation and interfacial instability. A combined strategy of bulk regulation and surface chemistry design is crucial to handle these issues. Here, we present a simultaneous $Li_2WO_4$-coated and gradient W-doped $0.98LiNi_{0.5}Mn_{0.5}O_2\cdot0.02Li_2WO_4$ cathode through modulating the content of the exotic dopant and stoichiometric lithium salt during lithiation calcination. Benefiting from the slightly Li-enriched chemistry induced by the hetero-epitaxially grown $Li_2WO_4$ surface, the $0.98LiNi_{0.5}Mn_{0.5}O_2\cdot0.02Li_2WO_4$ cathode demonstrates superior electrochemical performance to W-doped $LiNi_{0.49}Mn_{0.49}W_{0.02}O_2$ and $WO_3$ coated $0.98LiNi_{0.5}Mn_{0.5}O_2\cdot0.02WO_3$ cathodes without a Li-enriched phase. Specifically, when cycled in the potential range of 2.7–4.5 V at 30 °C, the $0.98LiNi_{0.5}Mn_{0.5}O_2\cdot0.02Li_2WO_4$ cathode possesses a high discharge capacity of 199.2 and 156.5 mA h $g^{-1}$ at 0.1 and 5C and a capacity retention of 92.88% after 300 cycles at 1C. Even at a high cut-off voltage of 4.6 V, it still retains a capacity retention of 91.15% after 200 cycles at 1C and 30 °C. Compared with $LiNi_{0.5}Mn_{0.5}O_2$, the enhanced performance of $0.98LiNi_{0.5}Mn_{0.5}O_2\cdot0.02Li_2WO_4$ can be attributed to its robust bulk and stable interface, inhibited lattice oxygen release, and improved $Li^+$ transport kinetics. Our work emphasizes the significance of the slightly Li-enriched chemistry and bulk modulation strategy in stabilizing cathodes and hence unlocks vast possibilities for future cathode design.

## 1. Introduction

Owing to their high specific capacity, $LiNiO_2$ and nickel-rich oxides such as $LiNi_xM_{1-x}O_2$ (where M = Mn, Co, Al, *etc.*) are highly promising cathodes for lithium-ion batteries with high energy density.[1–5] However, high Ni content also means high cost (necessary but costly Co and Ni), high risk under extreme conditions (fast charging, high voltage or high temperature operation, *etc.*) and inferior thermal safety.[6–8] Co-free alternatives such as $LiNi_{1-x}Mn_xO_2$, with a medium nickel content and appropriate manganese content, show enhanced structure stability due to the presence of $Ni^{2+}$/$Mn^{4+}$ charge separation.[9] In the solid solution system, $Ni^{2+}$ remains electrochemically active, and $Mn^{4+}$ acts as a stabilizer for the structure, leading to improved cycling performance and thermal stability compared to $LiNiO_2$.[10,11] To manage the defect of the low discharge capacity brought by decreased Ni content, high voltage operation has been proven efficient in embedding and releasing more lithium ions, thereby enhancing discharge capacity and overall energy density.

High voltage operation represents deep lithium-ion deintercalation and sufficient redox reactions of the active transition metal, which cause chemical instability for the interface and bulk structure.[12–14] The extraction of massive lithium ions would induce the generation of lithium vacancies followed by the transfer of transition metal ions to lithium sites, further aggravating cation disorder.[15–18] In addition, the deepened delithiation reaction would intensify the volume expansion and contraction of the layered structure.[19,20] More importantly, the deep redox reaction could generate more highly reactive and unstable $Ni^{4+}$, which tends to obtain electrons to form $Ni^{2+}$, especially at the surface of the cathode materials. This behavior would induce the release of lattice oxygen, resulting in a phase

---

[a] College of Materials and Chemistry & Chemical Engineering, Chengdu University of Technology, Chengdu 610059, Sichuan, China. E-mail: xiangwei@cdut.edu.cn

[b] College of Chemistry and Materials Engineering, Wenzhou University, Wenzhou, 325035, PR China. E-mail: xiaoyao@wzu.edu.cn; xhl@cdut.edu.cn

[c] Research Institute of Frontier Science, Southwest Jiaotong University, Chengdu 610031, PR China

[d] Yibin Libode New Materials Co., Ltd, Yibin 644200, PR China

[e] Ruyuan HEC New Energy Materials Co., Ltd, Ruyuan 512700, PR China

[f] Institute of Energy Materials Science, University of Shanghai for Science and Technology, Shanghai 200093, PR China

[g] Tianfu Yongxing Laboratory, Chengdu 610213, PR China

† Electronic supplementary information (ESI) available. See DOI: https://doi.org/10.1039/d4sc03805c

transition from layered to spinel and then to a rock salt phase.[20–23] What's more, oxygen loss gradually penetrates the bulk of active particles, destroying the structural stability of the crystal. A similar phenomenon happened at high-temperature operation; faster lithiation/delithiation reactions and chaotic mass transfer at the electrode/electrolyte interface would also amplify the possibility of parasitic side reactions,[24] gas release and local heating runaway.[25,26] Hence, it is urgent to develop a rational and feasible strategy to enhance the bulk and interfacial stability, improving the cycling stability and rate capability of the cathode.

Since structure collapse always occurs at the crystal surface during high voltage operation, reported strategies, such as lattice doping and surface coating, are expected to retain the integrity of the cathode. In the former situation, exotic atoms, including Al, Ti, Nb, W, Mo, *etc.*, are likely to be introduced to the crystal lattice near the particle's surface, promoting the structure robustness of the material during extended cycles.[27–30] Lately, a family of W-doped Ni-rich cathodes has displayed improved cycle performance and thermal and structural stability.[19,21,23,31–34] However, introducing electrochemically inert elements would cause capacity reduction. Although high-valent dopants could effectively trap labile oxygen in the layered structure, the introduction of some high-valent dopants also induces harmful cation mixing near the surface, which is detrimental for $Li^+$ exchange.[19,31,35] Thus, rational design should be considered to reduce capacity loss and alleviate harmful cation mixing caused by high-valent dopants. The latter surface coating with good mechanical strength could dramatically improve the interface properties of layered oxides by avoiding direct contact between the electrode and electrolyte. Except for mechanic strength, another critical factor is the limited $Li^+$ transfer rate across the interface induced by coatings.[36] Following this trend, a fast lithium-ion conductor tends to be selected owing to its high lithium-ion transfer coefficient.[37–39] For the mechanism of lattice doping and surface coating in the enhancement of $Li^+$ lithiation/delithiation, it's not difficult to see that most lattice doping works on the bulk, while surface coating places special emphasis on the surface/interface characters, whereas, the discrepancy between lattice doping and surface coating is not clear enough. Following this trend, the surface coating and doping integrated strategy is an ideal choice to save layered oxides from predicament. Considering the complex synthesis of layered cathodes and surface reactivity of layered oxides with moisture/air, easily scalable routes should be taken into consideration. In this context, all in one design including gradient doping and surface chemistry modulating should be adopted to enhance the electrochemical performance of Ni/Mn based layered oxides.

Therein, we designed simultaneous gradient W doped and $Li_2WO_4$-coated $0.98LiNi_{0.5}Mn_{0.5}O_2\cdot 0.02Li_2WO_4$ cathodes by modulating the content of the exotic dopant and stoichiometric lithium salt during calcination. Pristine $LiNi_{0.5}Mn_{0.5}O_2$, W doped $LiNi_{0.5}Mn_{0.5}O_2$ and $WO_3$ coated $LiNi_{0.5}Mn_{0.5}O_2$ cathodes were prepared as references to reveal the working mechanism of the $0.98LiNi_{0.5}Mn_{0.5}O_2\cdot 0.02Li_2WO_4$ cathode. Compared with W doped or $WO_3$ coated cathodes without a Li-enriched phase, the $0.98LiNi_{0.5}Mn_{0.5}O_2\cdot 0.02Li_2WO_4$ cathode with a gradient W doped lattice and uniform $Li_2WO_4$ coated surface demonstrates superior electrochemical performance. This work resolves the two knotty issues of crystal stability and interfacial stability of high-voltage cathodes and emphasises the significance of a slightly Li-enriched surface/interface for high-energy cathodes.

## 2. Results and discussion

A series of $(1-x)LiNi_{0.5}Mn_{0.5}O_2\cdot xLi_2WO_4$ ($x = 0$, 0.01, 0.02, 0.03, 0.05; denoted as NM50, NM50-LW1, NM50-LW2, NM50-LW3, and NM50-LW5) cathodes, along with $LiNi_{0.49}Mn_{0.49}W_{0.02}O_2$ (NM50-W2) and $0.98LiNi_{0.5}Mn_{0.5}O_2\cdot 0.02WO_3$ (NM50-WO2) cathodes, were synthesized by a high-temperature solid-state method using a co-precipitated $Ni_{0.5}Mn_{0.5}(OH)_2$ precursor. As shown in Fig. S1,† the $Ni_{0.5}Mn_{0.5}(OH)_2$ precursor and subsequent calcined cathodes consist of spherical secondary particles composed of agglomerated lamellar primary particles. When $x$ exceeds 0.03, the coating layer becomes visible on the surface of particles.

X-ray diffraction (XRD) patterns of NM50, NM-W2, NM50-LW1, NM50-LW2, NM50-LW3, NM50-LW5 and NM-WO2 show that all peaks correspond to the layered $\alpha$-$NaFeO_2$ structure with a space group of $R\bar{3}m$ (Fig. 1a and S2†).[40,41] Notably, the peak positions of (003) and (104) reflections gradually shift to lower angles and $Li_2WO_4$ peaks become stronger as the amount of $Li_2WO_4$ increases, indicating the bigger $d$ spacing for (003)/(104) and the formation of $Li_2WO_4$ in the modified cathodes. Additionally, the shift of the (003) peak for NM50-W2, NM50-LW2 and NM50-WO2 to lower angles indicates that the (003) layer spacing of the modified cathodes is wider than that of NM50 (Fig. S3†). XRD Rietveld refinement and the corresponding lattice parameters are presented in Fig. 1b, c, S4 and Table S1.† Considering the relatively larger radius of $W^{6+}$ (0.60 Å for $W^{6+}$ *vs.* 0.56 Å for $Ni^{3+}$ and 0.53 Å for $Mn^{4+}$), the increase of the $c$-axis for the W modified cathodes suggests the successful incorporation of W into the lattice of the crystal.[34,42] Moreover, antisite defects where Ni atoms occupy Li sites were determined to be 8.6%, 8.1%, 7.3%, and 8.2% for NM50, NM50-W2, NM50-LW2, and NM50-WO2, respectively. And the cation mixing of NM50-LW1, NM50-LW2, NM50-LW3, and NM50-LW5 is lower than that of NM50, indicating the positive effect of $Li_2WO_4$ on the ordered layered structure.[19,29]

X-ray photoelectron spectroscopy (XPS) was utilized to investigate the valence states and relative content of the elements in NM50 and NM50-LW2 (Fig. 1d–g and S5†). Compared with pristine NM50, NM50-LW2 exhibits a reduced content of surface oxygen and a higher content of lattice oxygen (Fig. S5b and c†), which can be attributed to the stabilized active surface by the $Li_2WO_4$ layer. Additionally, the peak area of C–O–C and O–C=O for NM50-LW2 is smaller than that for NM50, suggesting reduced residual Li compounds (such as $Li_2CO_3$) after $Li_2WO_4$ modification. Compared with the absence of the W 4f signal for NM50, an obvious W 4f signal can still be detected for NM50-LW2 after etching for 90 s (Fig. 1f and S5d†). The shift of Ni 2p and Mn 2p core levels to lower binding energy indicates

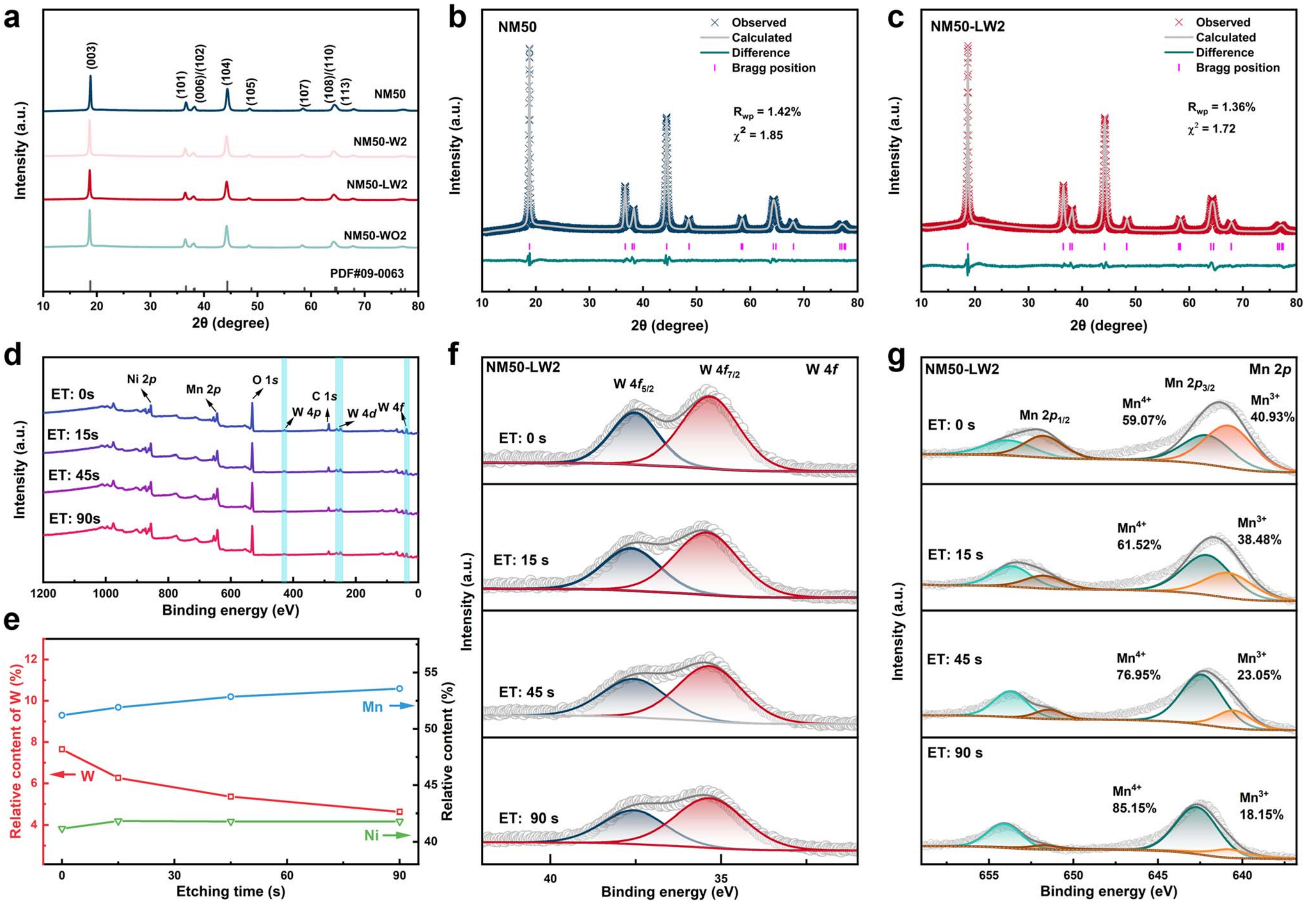

Fig. 1 (a) XRD pattern of NM50, NM50-W2, NM50-LW2, and NM50-WO2; (b and c) Rietveld refinements of the XRD pattern of NM50 (b) and NM50-LW2 (c). (d) XPS full spectrum of NM50-LW2 obtained with different etching times; (e) relative content of Ni, Mn and W elements obtained by XPS with different etching times; (f and g) XPS depth profiles of W 4f (f) and Mn 2p (g) with different etching times.

that the content of $Mn^{3+}$ and $Ni^{2+}$ in NM50-LW2 is higher than that in NM50 (Fig. S5e and f†), which is due to the charge compensation induced by $W^{6+}$ gradient doping.[43] According to the relative content of Ni, Mn and W obtained after different etching times, the W content gradually decreases, while the Mn and Ni content increases from the surface to the inside, confirming the gradient distribution of W inside the crystal (Fig. 1e and f). Furthermore, the Mn 2p peak gradually shifts towards higher binding energy (Fig. 1g), suggesting a progressive increase in the valence state of Mn from the surface to the bulk, which further verifies the gradient distribution of $W^{6+}$ from the surface to the bulk structure.

High angle annular dark field scanning transmission electron microscopy (HAADF-STEM) was employed to characterize the microstructure of NM50 and NM50-LW2. As shown in Fig. 2a, a continuous phase transition from the ordered layered phase to the disordered rock salt phase can be observed from the inside to the surface region of NM50. The transition metal layers are distinctly discernible inside NM50, with a layer spacing of $d = 4.73$ Å, corresponding to the (003) crystal plane of the layered phase. Fast Fourier transform (FFT) analysis confirms that this region belongs to the $R\bar{3}m$ space group (Fig. 2a(I)). In the subsurface region, a defective spinel-like structure, with transition metals occupying lithium sites gradually emerges (Fig. 2a(II)). Ultimately, the phase in the surface region transforms into a disordered $Fm\bar{3}m$ rock salt structure (Fig. 2a(III)). In contrast, NM50-LW2 exhibits a phase transition from the ordered layered phase to a slightly disordered layered structure, and a coating layer approximately 5 nm can be observed in the outer surface region (Fig. 2b). The bulk phase of NM50-LW2 demonstrates a clear layered structure, with the layer spacing $d = 4.78$ Å, which corresponds to the (003) crystal plane of the layered phase (Fig. 2b(I)). The larger layer spacing of NM50-LW2 than that of NM50 could be attributed to the incorporation of larger $W^{6+}$ into the lattice, which generates wider channels for rapid $Li^+$ diffusion and ensures structural stability during repeated $Li^+$ insertion/extraction.[44–50] Compared with NM50, a significant alleviation of $Li^+/Ni^{2+}$ cation mixing could be observed for the subsurface region of NM50-LW2 (Fig. 2b(II)). This improvement is possibly due to the Li-enriched conditions, which reduce the lithium vacancies near the surface region and inhibit migration of $Ni^{2+}$ to the lithium layer in the corresponding region. Fig. 2b(III) provides a magnified view of the outer surface region of NM50-LW2.

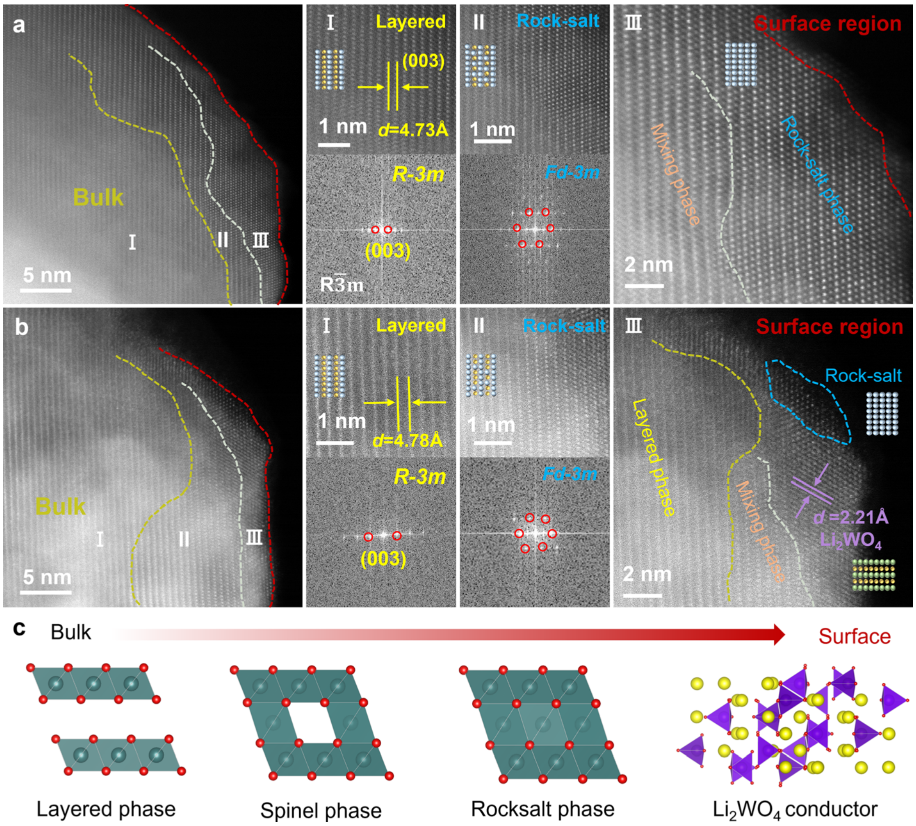

Fig. 2 (a and b) High-angle annular dark-field (HAADF) and fast Fourier transform (FFT) images of NM50 (a) and NM50-LW2 (b). (c) Schematic diagram of the phase transitions for NM50-LW2 from the bulk to the surface.

Obviously, there exists a hetero-epitaxially grown coating layer with a distinguishing layer spacing of $d = 2.21$ Å, which corresponds to the (152) crystal plane of $Li_2WO_4$, further confirming the successful construction and integration of $Li_2WO_4$. Thus, it can be concluded that the phase of NM50-LW2 transitions from a W doped layered phase to a spinel phase, then to a rock salt phase and finally to a $Li_2WO_4$ compound from the bulk to the surface (Fig. 2c).

The electrochemical performance of the cathodes was evaluated using a half cell in the potential range of 2.7–4.5 V at 30 °C using galvanostatic charging/discharging (GCD) tests with 1C defined as 170 mA $g^{-1}$. As shown in Fig. S6,† from the consideration of discharge capacity, rate capacity and cycle life, NM50-LW2 shows relatively superior electrochemical performance among the cathodes $(1-x)LiNi_{0.5}Mn_{0.5}O_2\cdot xLi_2WO_4$ ($x = 0$, 0.01, 0.02, 0.03, 0.05) with various $Li_2WO_4$ contents. Obviously, excessive $Li_2WO_4$ would hinder the insertion/extraction of $Li^+$ and goes against the electrochemical performance. In addition, as shown in Fig. 3a, NM50-LW2 also exhibits a much higher initial discharge capacity (199.17 mA h $g^{-1}$) and initial coulombic efficiency (95.32%) than NM50 (196.97 mA h $g^{-1}$ and 90.72%), NM50-W2 (191.27 mA h $g^{-1}$ and 91.64%), and NM-WO2 (195.08 mA h $g^{-1}$ and 93.54%). As shown in Fig. 3b, NM50-LW2 shows much improved rate performance than NM50, NM50-W2, and NM-WO2. At 5C, a high discharge capacity of 156.5 mA h $g^{-1}$ can still be obtained for NM50-LW2, which outperformed 113.3 mA h $g^{-1}$ for NM50, 137.6 mA h $g^{-1}$ for NM50-W2, and 152.1 mA h $g^{-1}$ for NM50-WO2. As shown in Fig. 3c, NM50-LW2 exhibits a superior capacity retention of 92.88% and a discharge capacity of 170.8 mA h $g^{-1}$ after 300 cycles at 1C in the potential range of 2.7–4.5 V, which outperformed 87.01% and 152.3 mA h $g^{-1}$ for NM50, 91.67% and 162.7 mA h $g^{-1}$ for NM50-W2, and 91.84% and 165.7 mA h $g^{-1}$ for NM50-WO2. When cycled at a high temperature of 55 °C, NM50-LW2 still possesses a capacity retention of 91.44% after 300 cycles (Fig. 3d), which is higher than 85.10% for NM50, 88.59% for NM50-W2 and 86.07% for NM50-WO2. Moreover, when cycled in the potential range of 2.7–4.6 V at 1C and 30 °C (Fig. 3e), NM50-LW2 can still exhibit a capacity retention of 91.15% after 200 cycles, which is higher than 88.39% for NM50, 90.81% for NM50-W2 and 90.05% for NM50-WO2. To further verify the excellent electrochemical performance induced by the slightly Li-enriched chemistry, the cycle performance of NM50-LW2 and NM50 was also measured using a full cell with graphite as the anode in the voltage range of 2.7–4.5 V at 1C and 30 °C. As shown in Fig. 3f, after 500 cycles, NM50-LW2 still exhibits a capacity of 169.4 mA h $g^{-1}$, with a superior capacity retention of 97.47%, confirming the excellent cycle stability provided by the slightly Li-enriched chemistry. However, NM50 only exhibits a capacity of 118.9 mA h $g^{-1}$, with a relatively lower capacity retention of 69.41%, which is significantly lower than that exhibited by NM50-LW2.

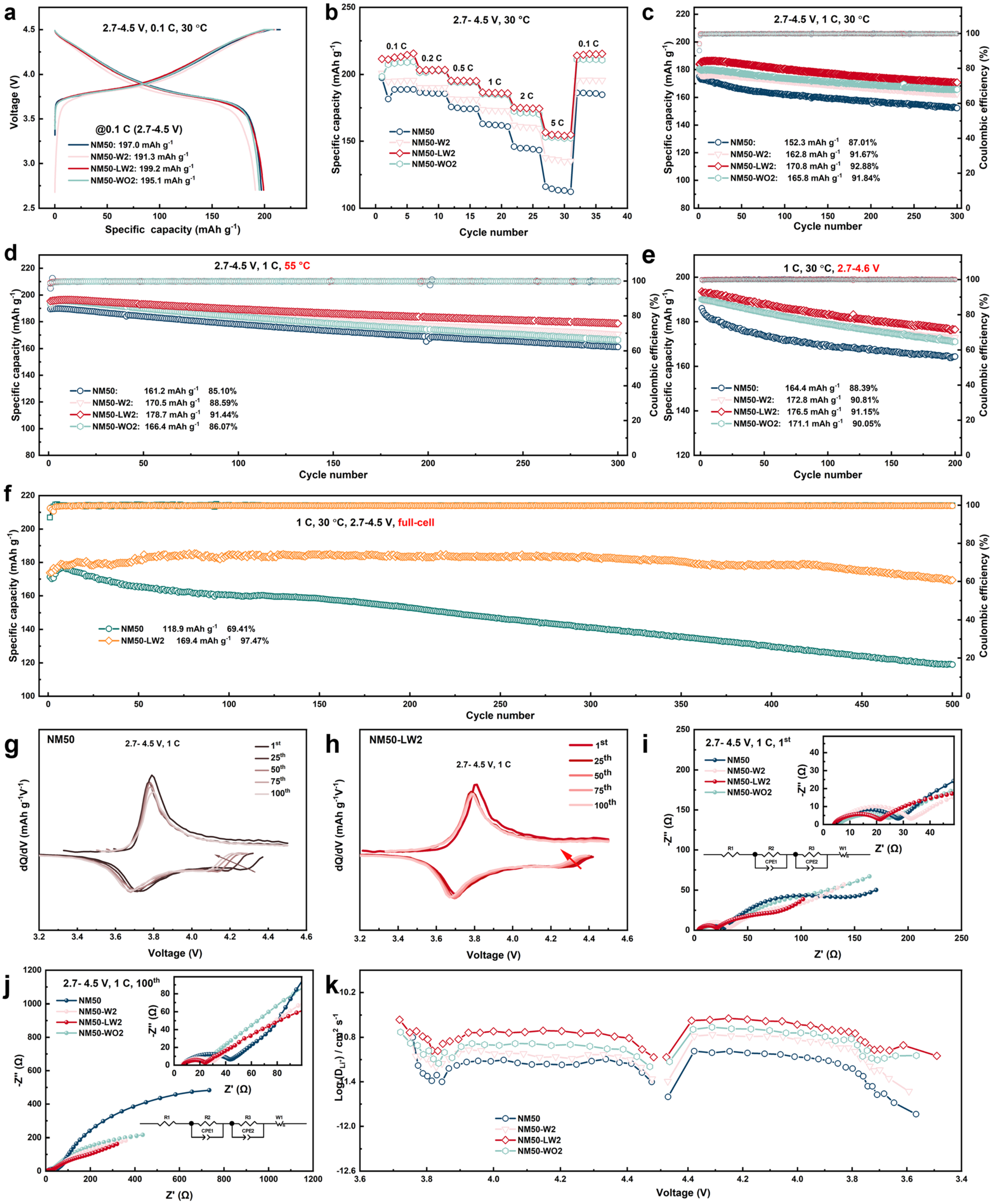

Fig. 3 (a–e) The initial charging/discharging curve at 0.1C (a), rate capacity (b), and cycling performance of NM50, NM50-W2, NM50-LW2 and NM50-WO2 at 1C in the potential range of 2.7–4.5 V at 30 °C (c), at 1C in the potential range of 2.7–4.5 V at 55 °C (d), and at 1C in the potential range of 2.7–4.6 V at 30 °C (e). (f) Cycle performance of NM50-LW2 and NM50 in a full cell in the voltage range of 2.7–4.5 V at 1C and 30 °C. (g and h) The d*Q*/d*V* curves of NM50 (g) and NM50-LW2 (h). (i and j) Nyquist plots of NM50, NM-W2, NM50-LW2 and NM50-WO2 after one cycle (h) and 100 cycles (i); (k) $Li^+$ diffusion coefficient of NM50, NM50-W2, NM50-LW2 and NM50-WO2 during the charge and discharge process.

A comparison of the electrochemical performance of the cathodes reveals that both W doping and the slightly Li-enriched conditions are crucial for designing stable Ni/Mn layered oxides. Although 2 mol% $WO_3$ coating and W doping both can enhance the cycling stability of the cathode, 2 mol% $WO_3$ coating appears more effective for the enhancement of performance than W doping under mild conditions. However, under extreme conditions, the enhanced structural stability from lattice doping becomes more significant for long-term cycling. In our previous work, we also verified that surface stability is more critical than bulk stress-induced microcracks for long-life cycling in nickel-rich cathodes.[51] Modification simply by doping can enhance the structure stability of $LiNi_{0.5}Mn_{0.5}O_2$ but it doesn't create a stable surface to prevent electrolyte corrosion and metal dissolution. An inert $WO_3$ coating layer can act as a robust barrier to isolate the cathode from the electrolyte but does not modify bulk structural properties. However, direct $WO_3$ coating with a short calcination duration can induce lithium-deficient phases in the surface region due to the combination of W and $Li^+$ to form $Li_xW_yO_z$ compounds, leading to capacity attenuation.[52] By modulating the content of the exotic dopant and stoichiometric lithium salt during lithiation calcination, the surface-enriched W element combines with $Li^+$ to produce $Li_2WO_4$ compounds, forming a thin $Li^+$ conductor layer and a slightly Li-enriched chemistry in the subsurface region, endowing NM50-LW2 with a robust bulk lattice and surface region as well as superior cycle stability.

The d$Q$/d$V$ curves of the cathodes (Fig. 3g, h and S7†) across various cycles show a gradual shift of the oxidation peak to higher potential and a slight shift of the reduction peak to lower potential, indicating increased potential polarization due to structural degradation and surface-interface deterioration. Among these, NM50-LW2 demonstrates the smallest change, indicating the enhanced phase transition reversibility and stability introduced by $Li_2WO_4$. Moreover, the excellent structure stability of NM50-LW2 could be verified by the disparity in charge/discharge median voltage. As plotted in Fig. S8,† after 200 cycles NM50-LW2 only shows a small value of 0.189 V for the disparity in charge/discharge median voltage, which is far less than 0.241 V for NM50 and 0.201 V for NM50-W2. Nyquist plots of the cathodes after one cycle and 100 cycles were obtained and fitted to reveal the resistance evolution (Fig. 3i, j, S8b, S9 and Table S2†). Each curve consists of two semicircles and a slant line. The first semicircle in the high-frequency region, the second semicircle in the middle-frequency region, and the slant line in the low-frequency region represent the interface impedance ($R_{sf}$), charge transfer resistance ($R_{ct}$), and Warburg impedance, respectively.[53] Among these electrodes, NM50 shows the highest $R_{sf}$ and $R_{ct}$ values (42.81 and 528.6 Ω) after 100 cycles, followed by NM50-W2 (28.69 and 207.8 Ω), NM50-

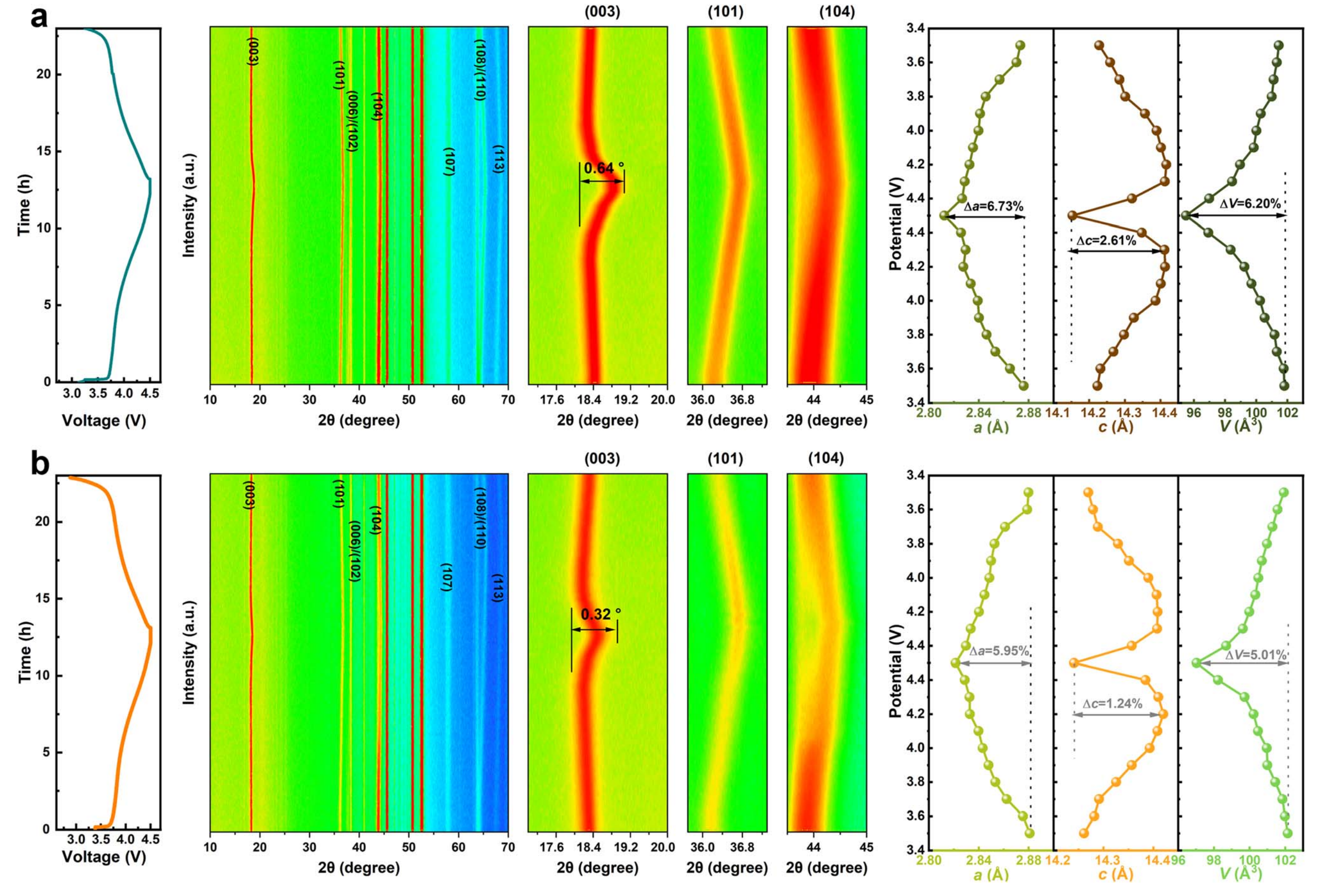

Fig. 4 GCD curve (left), *in situ* XRD patterns, selected enlarged peak (medium) and corresponding variation of cell parameters (right) for NM50 (a) and NM50-LW2 (b).

WO2 (26.92 and 241.6 Ω), and NM50-LW2 (24.88 and 184.7 Ω). The lowest $R_{sf}$ and $R_{ct}$ values for NM50-LW2 can be attributed to the surface $Li_2WO_4$ coating and the enlarged layer spacing in the layered bulk. The galvanostatic intermittent titration technique (GITT) was used to examine $Li^+$ diffusion kinetics during lithiation/delithiation. Obviously, the average lithium diffusion rate of NM50-LW2 during the charging/discharging process is significantly higher than that of NM50, NM50-W2, and NM50-WO2, indicating that the modification facilitates quick $Li^+$ migration (Fig. 3k).

To identify the structural evolution of NM50 and NM50-LW2 during the first cycle, *in situ* XRD was performed (Fig. 4). The (003) peak of NM50 and NM50-LW2 cathodes shifts to lower angles when charged from 2.7 to 4.3 V, labeling a gradual *c*-axis expansion. This can be attributed to a weakened shielding effect of the Li layer, which increases the repulsion between layers and subsequently enlarges the space for the Li–O layer.[54] At around 4.3 V, as more lithium-ions are extracted from the lattice, the charge is equalized by oxidizing TM ions, leading to a sharp shrink in the TM–O layer spacing, that is the main reason for particle pulverization and microcrack generation.[12,55] Additionally, NM50-LW2 almost completely returns to its original 2*θ* position after discharging, while NM50 shows a smaller offset. The maximum angular displacement of the (003) peak in NM50 (0.64°) is wider than that in NM50-LW2 (0.32°), suggesting that $Li_2WO_4$ surface modification and W-doping can effectively alleviate volume strain. The calculated lattice parameters from *in situ* XRD refinement, as a function of the charging state, show that the maximum *c*-axis shrinkage ($\Delta c$) of NM50 (2.61%) is higher than that of NM50-LW2 (1.79%). Additionally, the *a*-axis shrinkage degree ($\Delta a$) of NM50 and NM50-LW2 is 6.73% and 5.95%, respectively, further demonstrating that NM50-LW2 experiences less lattice distortion.[56,57] The smaller pronounced lattice changes of NM50-LW2 demonstrate that the phase transition reversibility and stability are enhanced after introducing $Li_2WO_4$.

*In situ* differential electrochemical mass spectrometry (DEMS) was utilized to monitor the internal gas generation during the charging process (Fig. 5a and b). Without any modification, pristine NM50 releases $O_2$ and $CO_2$ gases after charging to 4.3 V. In contrast, the emission of $O_2$ and $CO_2$ gases was entirely restrained in NM50-LW2. The thermal stability of

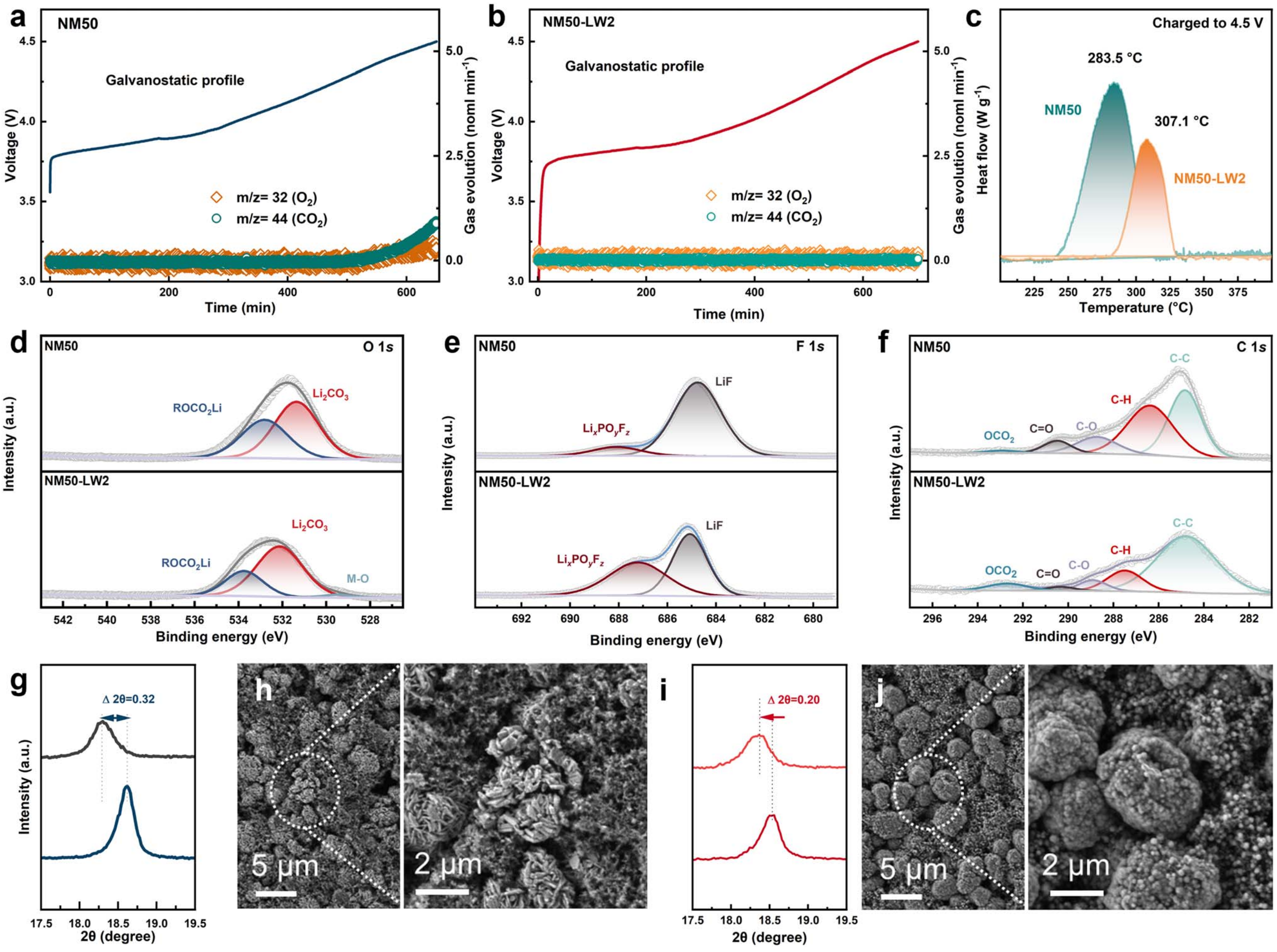

Fig. 5 (a and b) *In situ* DEMS measurements of NM50 (a) and NM50-LW2 (b). (c) DSC measurements of NM50 and NM50-LW2 charged to 4.5 V. (d–f) XPS profiles of O 1s (d), F 1s (e), and C 1s (f) for NM50 and NM50-LW2 cathodes after 300 cycles. (g–j) Enlarged (003) reflections and SEM images of NM50 (g and h) and NM50-LW2 (i and j) after 300 cycles.

the fully charged NM50 and NM50-LW2 electrodes was also examined using differential scanning calorimetry (DSC) (Fig. 5c). The NM50-LW2 electrode exhibited a higher exothermic peak at 307.1 °C and a lower heat release of 71.38 J $g^{-1}$, which are superior to 283.5 °C and 131.5 J $g^{-1}$ exhibited by NM50. This indicates the reinforced stability provided by the surface lithium-rich $Li_2WO_4$ coating and gradient W-doped bulk and is consistent with the improved cycling performance at high temperature. Subsequently, XPS analysis of NM50 and NM50-LW2 after 300 cycles was conducted to gain further insights into the chemical composition of the cathode–electrolyte interface (CEI) layer near the cathode surface. In the O 1s spectrum (Fig. 5d), compared with NM50-LW2, the area of the $ROCO_2Li$ peak in NM50 is larger, suggesting that more severe electrolyte decomposition occurred in NM50. Notably, the TM–O peak is well-detected in NM50-LW2 but absent in NM50, indicating that a thinner CEI film forms on the surface of NM50-LW2. In addition, as shown in Fig. 5e, the content of LiF in NM50 is significantly higher than that in NM50-LW2. Moreover, the C–O and C═O peaks in NM50-LW2 are smaller than those in NM50 (Fig. 5f), further demonstrating that the surface $Li_2WO_4$ coating and W-doped bulk inhibit side reactions.

The XRD patterns and SEM of the cycled electrodes were obtained to uncover the phase and morphology evolution of the cathodes during extended cycling. The XRD results (Fig. 5g and i) show that the (003) peak of NM50 exhibits a pronounced left shift with an offset of 0.32°, likely attributed to Li loss and corresponding phase degradation. In comparison, the shift magnitude of the (003) peak in NM50-LW2 (0.20°) is narrower, indicating a well-maintained layered structure. Within the repetitive charge–discharge process, the accumulation of anisotropic contraction/expansion in lattice parameters would induce breakage for secondary particles to buffer the volume strain. However, this breakage exposes more active surfaces to electrolyte, exacerbating side reactions and capacity fading.[58] SEM images of NM50 and NM50-LW2 after 300 cycles demonstrate that NM50 has obvious microcracks, whereas NM50-LW2 basically maintains its sphere-like morphology without apparent microcracks (Fig. 5h and j). Therefore, the surface lithium-rich $Li_2WO_4$ coating and gradient doping integrated strategy strengthens the interface robustness and mitigates the strain aggregation. These results further support the surface Li-enriched $Li_2WO_4$ coating and gradient W-doping strategy could efficaciously alleviate structural degradation during long cycling.

In short, all W-modified materials demonstrate superior electrochemical performance compared to pristine $LiNi_{0.5}Mn_{0.5}O_2$. Specifically, $0.98LiNi_{0.5}Mn_{0.5}O_2\cdot 0.02Li_2WO_4$ exhibits outstanding electrochemical performance under extreme conditions (Table S3†). The enhanced electrochemical performance of W-modified cathodes indicates that both lattice doping and surface coating are essential for improving the cycling stability and maintaining the bulk integrity of Ni/Mn based layered oxides. Although the direct introduction of $WO_3$ coating or a W dopant during lithiation calcination can create W-rich surface regions on the surface of primary grains, the surface phase usually contains Li–W–O compounds and Li-poor regions due to the lack of stoichiometric Li sources. The surface lithium-deficient phase due to the lithium despoilment induced by W would inevitably intensify cation disordering and relatively inferior regions (Fig. 6a and b). In contrast, benefiting from the modulated content of the W dopant and stoichiometric lithium salt during lithiation calcination, a W-doped lattice and a Li-enriched surface region induced by hetero-

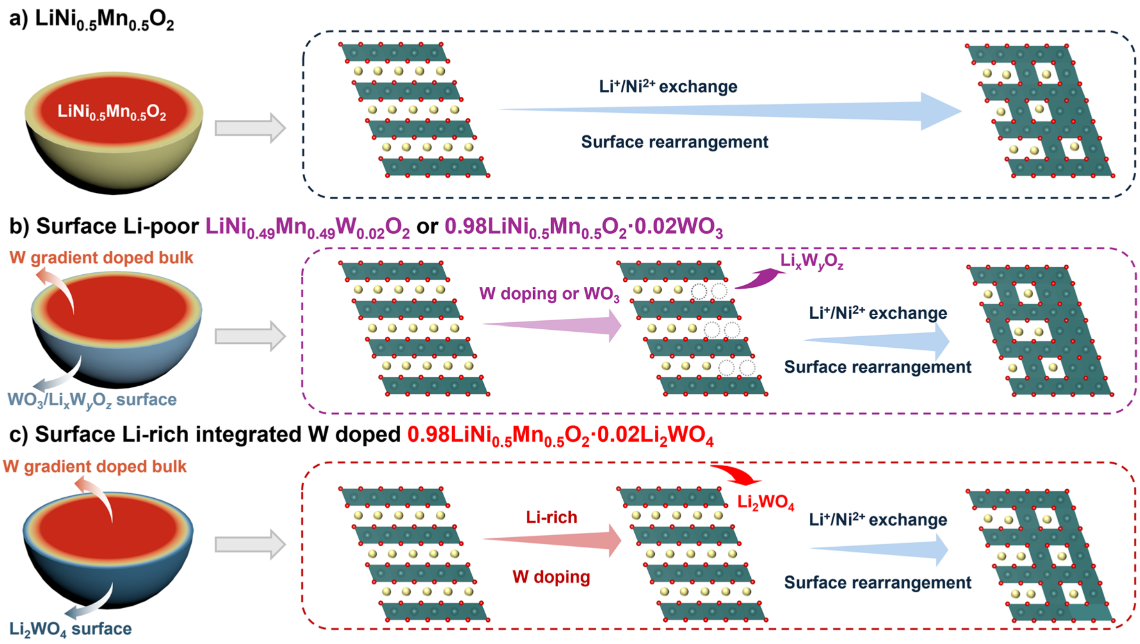

Fig. 6 Schematic diagram for the mechanism of $LiNi_{0.5}Mn_{0.5}O_2$ (a), surface Li-poor $LiNi_{0.49}Mn_{0.49}W_{0.02}O_2$ or $0.98LiNi_{0.5}Mn_{0.5}O_2\cdot 0.02WO_3$ (b) and surface Li-enriched $0.98LiNi_{0.5}Mn_{0.5}O_2\cdot 0.02Li_2WO_4$ (c) during delithiation.

epitaxially grown $Li_2WO_4$ would result in reduced cation disordering and enhanced structure stability during extended cycles (Fig. 6c). Kinetics measurements and structural evolution demonstrate that the Li-enriched surface and gradient doping strategy significantly facilitate lithium-ion conduction, alleviate strain accumulation, reduce parasitic side reactions from electrolyte decomposition, and improve the lattice O stability in high cut-off voltage and high temperature operation.

## 3. Conclusions

In summary, a series of cathodes including $LiNi_{0.5}Mn_{0.5}O_2$, $(1-x)LiNi_{0.5}Mn_{0.5}O_2\cdot xLi_2WO_4$ ($x$ = 0, 0.01, 0.02, 0.03, 0.05), $LiNi_{0.49}Mn_{0.49}W_{0.02}O_2$, and $0.98LiNi_{0.5}Mn_{0.5}O_2\cdot 0.02WO_3$ were synthesized to investigate the role of Li-enriched conditions in the performance of Ni–Mn binary cathodes in high voltage/high temperature operation. Compared with lithium-deficient conditions induced by W doping and $WO_3$ coating, the combination of a slightly Li-enriched $Li_2WO_4$ surface coating and gradient W-doping strategy can significantly enhance the performance of the $0.98LiNi_{0.5}Mn_{0.5}O_2\cdot 0.02Li_2WO_4$ cathode. Specifically, the $0.98LiNi_{0.5}Mn_{0.5}O_2\cdot 0.02Li_2WO_4$ cathode exhibits outstanding cycling performance even under harsh conditions, retaining 91.15% capacity after 200 cycles at 1C with a cut-off voltage of 4.6 V and maintaining 91.44% capacity after 300 cycles at elevated temperature. This study offers a scalable approach to design high-energy-density and high-safety cathodes for next generation lithium-ion batteries.

## Data availability

The data supporting this article have been included as part of the ESI.†

## Author contributions

Siqi Chen: characterizations, investigation, formal analysis, writing – review & editing. Ping Zhang: characterizations. Xin Zhou: characterizations, investigation. Wenbin Wu: characterizations, investigation. Xiaohong Liu: editing, formal analysis. Yifeng Liu: editing. Guilin Feng: editing. Bin Zhang: supervision, resources. Wangyan Xing: supervision, resources. Meihua Zuo: supervision, resources. Ping Zhang: supervision, resources. Genpin Lv: resources. Yao Xiao: editing, formal analysis. Shixue Dou: resources. Wei Xiang: funding acquisition, supervision, investigation, resources, writing – review & editing, conceptualization, formal analysis.

## Conflicts of interest

There are no conflicts to declare.

## Acknowledgements

This work was financially supported by a project from the National Natural Science Foundation of China (21805018), the Sichuan Science and Technology Program (2022ZHCG0018, 2023NSFSC0117, and 2023ZHCG0060), the Yibin Science and Technology Program (2022JB005), TianfuYongxing Laboratory Organized Research Project Funding (2023KJGG13) and the project funded by the China Postdoctoral Science Foundation (2022M722704). Specifically, we thank Ceshigo (**https://www.ceshigo.com/**) and Zhinanzhen (**http://www.shiyanjia.com/**) for characterization measurements.

## References

1 J. T. Frith, M. J. Lacey and U. Ulissi, *Nat. Commun.*, 2023, **14**, 420.
2 J. Xiao, F. Shi, T. Glossmann, C. Burnett and Z. Liu, *Nat. Energy*, 2023, **8**, 329–339.
3 S.-T. Myung, F. Maglia, K.-J. Park, C. S. Yoon, P. Lamp, S.-J. Kim and Y.-K. Sun, *ACS Energy Lett.*, 2017, **2**, 196–223.
4 J. Xu, F. Lin, M. M. Doeff and W. Tong, *J. Mater. Chem. A*, 2017, **5**, 874–901.
5 E. M. Erickson, F. Schipper, T. R. Penki, J.-Y. Shin, C. Erk, F.-F. Chesneau, B. Markovsky and D. Aurbach, *J. Electrochem. Soc.*, 2017, **164**, A6341.
6 T. C. Liu, L. Yu, J. J. Liu, J. Lu, X. X. Bi, A. Dai, M. Li, M. F. Li, Z. X. Hu, L. Ma, D. Luo, J. X. Zheng, T. P. Wu, Y. Ren, J. G. Wen, F. Pan and K. Amine, *Nat. Energy*, 2021, **6**, 277–286.
7 W. D. Li, S. Lee and A. Manthiram, *Adv. Mater.*, 2020, **32**, 2002718.
8 W. E. Gent, G. M. Busse and K. Z. House, *Nat. Energy*, 2022, **7**, 1132–1143.
9 Y. Xia, L. Zhou, K. Wang, C. Lu, Z. Xiao, Q. Mao, X. Lu, J. Zhang, H. Huang, Y. Gan, X. He, W. Zhang and X. Xia, *J. Solid State Electrochem.*, 2023, **27**, 1363–1372.
10 S. Y. Tsai and K. Z. Fung, *Molecules*, 2023, **28**, 794.
11 P. Periasamy and N. Kalaiselvi, *J. Power Sources*, 2006, **159**, 1360–1364.
12 S. H. Song, M. Cho, I. Park, J. G. Yoo, K. T. Ko, J. Hong, J. Kim, S. K. Jung, M. Avdeev, S. Ji, S. Lee, J. Bang and H. Kim, *Adv. Energy Mater.*, 2020, **10**, 2000521.
13 Y. W. Mao, X. L. Wang, S. H. Xia, K. Zhang, C. X. Wei, S. Bak, Z. Shadike, X. J. Liu, Y. Yang, R. Xu, P. Pianetta, S. Ermon, E. Stavitski, K. J. Zhao, Z. R. Xu, F. Lin, X. Q. Yang, E. Y. Hu and Y. J. Liu, *Adv. Funct. Mater.*, 2019, **29**, 1900247.
14 P. F. Yan, J. M. Zheng, M. Gu, J. Xiao, J. G. Zhang and C. M. Wang, *Nat. Commun.*, 2017, **8**, 14101.
15 D. Wang, R. Kou, Y. Ren, C.-J. Sun, H. Zhao, M.-J. Zhang, Y. Li, A. Huq, J. Y. P. Ko, F. Pan, Y.-K. Sun, Y. Yang, K. Amine, J. Bai, Z. Chen and F. Wang, *Adv. Mater.*, 2017, **29**, 1606715.
16 C. S. Yoon, H.-H. Ryu, G.-T. Park, J.-H. Kim, K.-H. Kim and Y.-K. Sun, *J. Mater. Chem. A*, 2018, **6**, 4126–4132.
17 W. Li, B. Song and A. Manthiram, *Chem. Soc. Rev.*, 2017, **46**, 3006–3059.
18 J. Zheng, Y. Ye, T. Liu, Y. Xiao, C. Wang, F. Wang and F. Pan, *Acc. Chem. Res.*, 2019, **52**, 2201–2209.
19 X. Wang, B. Zhang, Z. Xiao, L. Ming, M. Li, L. Cheng and X. Ou, *Chin. Chem. Lett.*, 2023, **34**, 10772.
20 D. Rathore, M. Garayt, Y. Liu, C. Geng, M. Johnson, J. R. Dahn and C. Yang, *ACS Energy Lett.*, 2022, **7**, 2189–2195.

21 L. Liu, Y. Zhao, G. Jiang, L. Shan, Z. Yang, Y. Ma, Y. Zhang, Q. Meng and P. Dong, *Nano Res.*, 2023, **16**, 9250–9258.

22 X. Liu, D. Ren, H. Hsu, X. Feng, G.-L. Xu, M. Zhuang, H. Gao, L. Lu, X. Han, Z. Chu, J. Li, X. He, K. Amine and M. Ouyang, *Joule*, 2018, **2**, 2047–2064.

23 U. H. Kim, D. W. Jun, K. J. Park, Q. Zhang, P. Kaghazchi, D. Aurbach, D. T. Major, G. Goobes, M. Dixit, N. Leifer, C. M. Wang, P. Yan, D. Ahn, K. H. Kim, C. S. Yoon and Y. K. Sun, *Energy Environ. Sci.*, 2018, **11**, 1271–1279.

24 O. Breuer, A. Chakraborty, J. Liu, T. Kravchuk, L. Burstein, J. Grinblat, Y. Kauffman, A. Gladkih, P. Nayak, M. Tsubery, A. I. Frenkel, M. Talianker, D. T. Major, B. Markovsky and D. Aurbach, *ACS Appl. Mater. Interfaces*, 2018, **10**, 29608–29621.

25 K. Meng, Z. Wang, H. Guo and X. Li, *Electrochim. Acta*, 2017, **234**, 99–107.

26 J. Wandt, A. T. S. Freiberg, A. Ogrodnik and H. A. Gasteiger, *Mater. Today*, 2018, **21**, 825–833.

27 Y. Cheng, X. Zhang, Q. Leng, X. Yang, T. Jiao, Z. Gong, M.-S. Wang and Y. Yang, *Chem. Eng. J.*, 2023, **474**, 145869.

28 H. H. Sun, U.-H. Kim, J.-H. Park, S.-W. Park, D.-H. Seo, A. Heller, C. B. Mullins, C. S. Yoon and Y.-K. Sun, *Nat. Commun.*, 2021, **12**, 6552.

29 U.-H. Kim, G.-T. Park, B.-K. Son, G. W. Nam, J. Liu, L.-Y. Kuo, P. Kaghazchi, C. S. Yoon and Y.-K. Sun, *Nat. Energy*, 2020, **5**, 860–869.

30 N. Liu, L. Chen, H. Wang, J. Zhao, F. Gao, J. Liu, J. Dong, Y. Lu, N. Li, Q. Shi, Y. Su and F. Wu, *Chem. Eng. J.*, 2023, **472**, 145113.

31 N. Zaker, C. Geng, D. Rathore, I. Hamam, N. Chen, P. Xiao, C. Yang, J. R. Dahn and G. A. Botton, *Adv. Funct. Mater.*, 2023, **33**, 2211178.

32 S. Yuan, H. Zhang, D. Song, Y. Ma, X. Shi, C. Li and L. Zhang, *Chem. Eng. J.*, 2022, **439**, 135677.

33 C. Geng, D. Rathore, D. Heino, N. Zhang, I. Hamam, N. Zaker, G. A. Botton, R. Omessi, N. Phattharasupakun, T. Bond, C. Yang and J. R. Dahn, *Adv. Energy Mater.*, 2021, **12**, 2103067.

34 H.-H. Ryu, K.-J. Park, D. R. Yoon, A. Aishova, C. S. Yoon and Y.-K. Sun, *Adv. Energy Mater.*, 2019, **9**, 1902698.

35 Q. Zhang, Q. Deng, W. Zhong, J. Li, Z. Wang, P. Dong, K. Huang and C. Yang, *Adv. Funct. Mater.*, 2023, **33**, 2301336.

36 Q. Shi, F. Wu, H. Wang, Y. Lu, J. Dong, J. Zhao, Y. Guan, B. Zhang, R. Tang, Y. Liu, J. Liu, Y. Su and L. Chen, *Energy Storage Mater.*, 2024, **67**, 103264.

37 S. Luo, F. Yang, Z. Xiong, Y. Wu, X. Ao, C. Li, Q. Chen and K. Wang, *Chem. Eng. J.*, 2022, **448**, 137663.

38 Z. Tan, Y. Li, X. Xi, S. Jiang, X. Li, X. Shen, P. Zhang and Z. He, *Nano Res.*, 2022, **16**, 4950–4960.

39 Y. Liu, Q. Wang, L. Chen, Z. Xiao, X. Fan, S. Ma, L. Ming, A. Tayal, B. Zhang, F. Wu and X. Ou, *Mater. Today*, 2022, **61**, 40–53.

40 C. X. Tian, F. Lin and M. M. Doeff, *Acc. Chem. Res.*, 2018, **51**, 89–96.

41 H. H. Ryu, K. J. Park, C. S. Yoon and Y. K. Sun, *Chem. Mater.*, 2018, **30**, 1155–1163.

42 J. Meng, L. Xu, Q. Ma, M. Yang, Y. Fang, G. Wan, R. Li, J. Yuan, X. Zhang, H. Yu, L. Liu and T. Liu, *Adv. Funct. Mater.*, 2022, **32**, 2113013.

43 G. T. Park, H. H. Ryu, N. Y. Park, C. S. Yoon and Y. K. Sun, *J. Power Sources*, 2019, **442**, 227242.

44 D. Rathore, C. Liang, E. Zsoldos, M. Ball, S. Yu, C. Yang, Q. Wang and J. R. Dahn, *J. Electrochem. Soc.*, 2023, **170**, 020520.

45 F. Klein, C. Pfeifer, P. Scheitenberger, L. Pfeiffer, D. Zimmer, M. Wohlfahrt-Mehrens, M. Lindén and P. Axmann, *J. Mater. Chem. A*, 2023, **11**, 5135–5147.

46 Z. Jing, S. Wang, Q. Fu, V. Baran, A. Tayal, N. P. M. Casati, A. Missyul, L. Simonelli, M. Knapp, F. Li, H. Ehrenberg, S. Indris, C. Shan and W. Hua, *Energy Storage Mater.*, 2023, **59**, 102775.

47 G. Ding, M. Yao, J. Li, T. Yang, Y. Zhang, K. Liu, X. Huang, Z. Wu, J. Chen, Z. Wu, J. Du, C. Rong, Q. Liu, W. Zhang and F. Cheng, *Adv. Energy Mater.*, 2023, **13**, 2300407.

48 T. Zhou, H. Wang, Y. Wang, P. Jiao, Z. Hao, K. Zhang, J. Xu, J.-B. Liu, Y.-S. He, Y.-X. Zhang, L. Chen, L. Li, W. Zhang, Z.-F. Ma and J. Chen, *Chem*, 2022, **8**, 2817–2830.

49 A. Liu, N. Phattharasupakun, R. Väli, D. Ouyang and J. R. Dahn, *J. Electrochem. Soc.*, 2022, **169**, 030538.

50 N. Phattharasupakun, M. M. E. Cormier, Y. Liu, C. Geng, E. Zsoldos, I. Hamam, A. Liu, M. B. Johnson, M. Sawangphruk and J. R. Dahn, *J. Electrochem. Soc.*, 2021, **168**, 110502.

51 X. Wang, X. Zhou, X. Liu, G. Feng, S. Wang, B. Zhang, P. Zhang, M. Zuo, W. Xing, W. Fan, H. Zhang, G. Lv and W. Xiang, *Chem. Eng. J.*, 2024, **488**, 150795.

52 F. Reissig, J. Ramirez-Rico, T. J. Placke, M. Winter, R. Schmuch and A. Gomez-Martin, *Batteries*, 2023, **9**, 245.

53 W. Xiong, Y. Liu, G. Zhu, Y. Wang and H. Zheng, *J. Energy Storage*, 2023, **73**, 109086.

54 G.-T. Park, N.-Y. Park, T.-C. Noh, B. Namkoong, H.-H. Ryu, J.-Y. Shin, T. Beierling, C. S. Yoon and Y.-K. Sun, *Energy Environ. Sci.*, 2021, **14**, 5084–5095.

55 X. Chao, J. R. Philip, J. Quentin and P. G. Clare, *Adv. Energy Mater.*, 2020, **11**, 2003404.

56 Z. Lu, J. Zhang, Q. Zhang, D. Wong, W. Yin, N. Zhang, Z. Chen, L. Gu, Z. Hu and X. Liu, *Adv. Sci.*, 2023, **10**, 2206442.

57 W. Li, H. Y. Asl, Q. Xie and A. Manthiram, *J. Am. Chem. Soc.*, 2019, **141**, 5097–5101.

58 H. Gao, X. Zeng, Y. Hu, V. Tileli, L. Li, Y. Ren, X. Meng, F. Maglia, P. Lamp, S.-J. Kim, K. Amine and Z. Chen, *ACS Appl. Energy Mater.*, 2018, **1**, 2254–2260.